Effect of Surface Microstructure on Electrochemical Performance of Garnet Solid Electrolytes

Lei Cheng,*[,†,‡] Wei Chen,[†] Martin Kunz,[§] Kristin Persson,[†] Nobumichi Tamura,[§] Guoying Chen,[†] and Marca Doeff*[,†]

[†]Lawrence Berkeley National Laboratory, Environmental Energy Technologies Division, University of California, Berkeley, California 94720, United States

[‡]Department of Material Sciences and Engineering, University of California, Berkeley, California 94720, United States

[§]Advanced Light Source, Lawrence Berkeley National Laboratory, University of California, Berkeley, California 94720, United States

Ⓢ Supporting Information

ABSTRACT: Cubic garnet phases based on Al-substituted $Li_7La_3Zr_2O_{12}$ (LLZO) have high ionic conductivities and exhibit good stability versus metallic lithium, making them of particular interest for use in next-generation rechargeable battery systems. However, high interfacial impedances have precluded their successful utilization in such devices until the present. Careful engineering of the surface microstructure, especially the grain boundaries, is critical to achieving low interfacial resistances and enabling long-term stable cycling with lithium metal. This study presents the fabrication of LLZO heterostructured solid electrolytes, which allowed direct correlation of surface microstructure with the electrochemical characteristics of the interface. Grain orientations and grain boundary distributions of samples with differing microstructures were mapped using high-resolution synchrotron polychromatic X-ray Laue microdiffraction. The electrochemical characteristics are strongly dependent upon surface microstructure, with small grained samples exhibiting much lower interfacial resistances and better cycling behavior than those with larger grain sizes. Low area specific resistances of 37 Ω cm^2 were achieved; low enough to ensure stable cycling with minimal polarization losses, thus removing a significant obstacle toward practical implementation of solid electrolytes in high energy density batteries.

KEYWORDS: solid electrolyte, interface, lithium metal, solid state battery, heterostructures
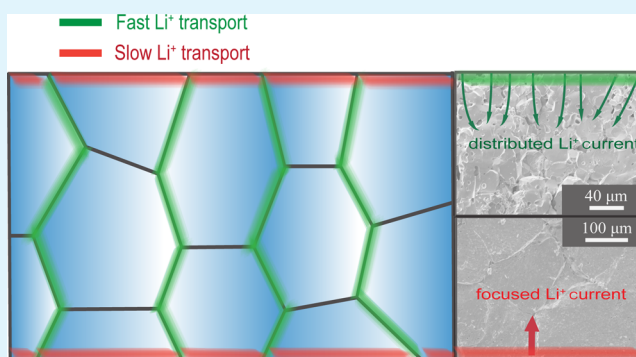
■ INTRODUCTION

Enabling cycling of lithium metal anodes is a critical step toward achieving breakthroughs in next generation rechargeable batteries, such as Li−air and Li−sulfur systems.[1−4] The use of a solid ceramic electrolyte on the anode has recently been proposed to mitigate the deleterious effects of lithium dendrite growth and mossy deposition associated with repeated plating and stripping of the lithium anode when conventional liquid or polymer electrolytes are used. A practical solid electrolyte must have high ionic conductivity, good chemical stability against metallic lithium, low interfacial resistance, and long cycling in order to realize high performance devices.[5] Despite superionic conductivities close to or even higher than conventional liquid electrolytic solutions, the practical application of $Li_{1+x}Al_x$-$Ti_{2-x}(PO_4)_3$ (LATP)[6,7] and $Li_{10}GeP_2S_{12}$ (LGPS)[8] is hindered by their instabilities against reduction by lithium metal.[9,10] In contrast, highly conductive garnet oxides[11,12] and thiophosphates exhibit better stability against reduction by lithium metal.[13,14] Yet, high interfacial resistances,[15−17] severe over potential build-up during cycling,[14,18] and short cycle life[19,20]

remain unsolved problems for their application in practical devices.

The above-mentioned problems are associated with sluggish ion transport in the interfacial regions,[21] inhomogeneity in potential−current distributions,[22] and detrimental current focusing during operation.[23] These ionic transport properties are intimately related to the microstructures and chemical compositions of polycrystalline ceramics electrolytes.[7] Al substituted $Li_7La_3Zr_2O_{12}$ (LLZO), for example, is densified through a sintering process involving high temperatures and lengthy heating times, with both lithium and aluminum contents sensitive to processing conditions.[15,17] Attempts to modify the microstructure by changing either synthetic routes or processing conditions inevitably lead to variations in composition of the resulting densified ceramic. This accounts for the wide distribution of chemical compositions and microstructures reported in the literature for LLZO sam-
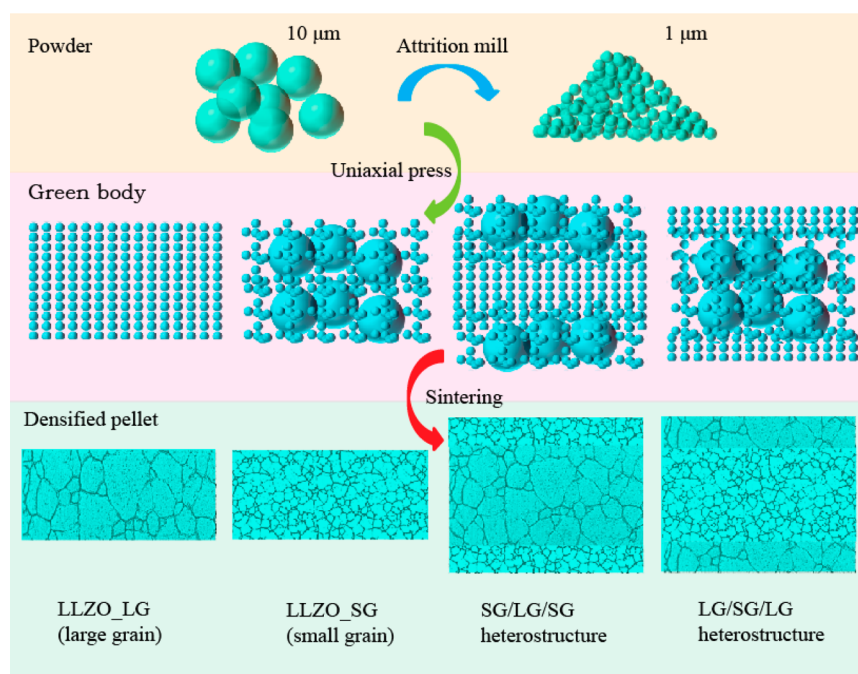
Figure 1. Schematic of ceramic processes for fabrication of LLZO pellets with large grains, small grains, and complex heterostructures with alternating large and small grain layer LLZO electrolytes. (Images of the densified heterostructures are for illustration purpose only and differ from the observed topologies of the actual pellets, provided in Figure 3.)

ples.[15,17,24−32] Despite the progress in microstructure engineering of solid state electrolytes, the knowledge of the relationships among microstructure, interfacial resistance, and cycling performance is very limited. The complexity involved in differentiating the roles of the interfaces and the bulk, as well as decoupling microstructure effects from those of chemical composition, presents formidable challenges in understanding the electrochemical behavior of solid electrolytes based on LLZO.

Herein we report a study that correlates electrolyte microstructure with interfacial and electrical cycling properties, using dense Al-substituted LLZO as a model system. Our approach was 3-fold: first, we developed a ceramic processing technique to prepare dense LLZO solid electrolytes with complex yet controllable microstructures, including both homo- and heterostructures, using the same sintering conditions; second, we demonstrated that the Li/LLZO interfacial resistance is strongly correlated with the interface microstructure and grain boundaries, and very low interfacial resistance can be achieved; and last, we differentiated the contributions from surfaces and bulk in symmetrical lithium cell measurements and revealed that the cycle life of LLZO is strongly impacted by the microstructure of the Li/LLZO interface, particularly the grain boundaries. Grain and grain boundary orientation mapping by high-resolution synchrotron X-ray Laue microdiffraction experiments indicated that grain boundaries play a critical role in the performance of solid electrolytes. Our work unveiled the correlation of key interfacial properties with solid electrolyte surface microstructures, providing insights into the optimization of polycrystalline ceramic electrolytes for durable high-rate, high-energy devices with lithium anodes.

■ EXPERIMENTAL SECTION

LLZO powder was synthesized via a solid state reaction as reported in ref 17. The as-synthesized fresh powder was ground by hand and sieved to below 75 μm to obtain particles 10 μm across. To prepare the 1 μm sized LLZO particles, some of the 10 μm LLZO powder was attrition milled at 450 rpm for 2 h with 2 mm diameter ZrO_2 media in isopropyl alcohol (IPA). IPA was removed by drying the samples in air under a heat lamp. Particle size analysis was carried out using a Beckman Coulter LS 200 particle characterization system.

The attrition-milled powder was mixed with 10 μm LLZO powder at varying ratios of 50, 70, 90, and 100 wt %. Pellets were made by cold uniaxial pressing of the powders using a 3/8 in. stainless steel dye without binder. LLZO bars were made by pressing fine powder into bar shapes and sintered at 1100 °C for 12 h in air. The dimensions of the bars were 16 mm × 3 mm × 2 mm. LLZO heterostructures were made by pressing the powders layer by layer using the same process. The pressed green bodies were placed on a LLZO powder bed, fully covered by fresh LLZO powder in a covered alumina tray, and then fired at 1100 °C for 12 h in air. Sintered pellets were stored in an Ar-filled glovebox. The surfaces of the sintered pellets were dry-polished using several pieces of polishing paper with grit numbers progressing from 240 to 600 in an Ar glovebox to avoid contact with air, water, and contamination from liquid polishing media. Special care was taken in polishing so that the surface layers were not fully removed in the heterostructured LLZO pellets. The densities were estimated from the weights and dimensions of the sintered LLZO circular disks. Powder samples and sintered pellets were characterized by X-ray powder diffraction (XRD) using a Bruker D2-Phaser with Cu Kα radiation (λ = 1.541 78 Å). The pure cubic LLZO pattern was simulated using PowderCell 2.4 (W. Kraus and G. Nolze, Federal Institute for Materials Research and Testing, Rudower Chaussee 5, 12489 Berlin, Germany) with unit cell parameters taken from the literature.[33] Surface and fractured cross-section images of the fresh pellets were obtained by scanning electron microscopy (SEM) using a JEOL-7500F field emission microscope or a HITACHI TM-1000 tabletop microscope, using secondary electron imaging (SEI) mode.

Alternating current impedance measurements were performed on dense pellets using a VMP3 multichannel potentiostat/galvanostat (Bio-Logic Science Instruments). For the experiments with blocking electrodes, gold layers were sputtered on both sides of the pellet, and Pt meshes and wires were attached as current collectors. For cells with nonblocking electrodes, soft metallic lithium was first spread on both

sides of the dense pellet to ensure good contact. Afterward, the pellet was sandwiched between two lithium foil disks in a Swagelok-type cell. The pressure was maintained in the Swagelok cells with springs having spring constants of 13.3N/cm, so that the maximum load was 17 N, corresponding to a pressure of 370 kPa. The estimated pressure on the Li/LLZO/Li cell was 200 kPa, considering the spring displacement. Samples were assembled in the same Swagelok cells with controlled displacement so that similar pressures were used for each.

Measurements were made at frequencies from 1 MHz to 1 Hz. The conductivities were calculated using the equation $\sigma = (1/Z)(L/A)$, where Z is the impedance, L is the pellet thickness, and A is the pellet area. An $(R_{pellet}Q_{pellet})(R_{interface}Q_{interface})$ equivalent circuit (see inset in Figure 4b) was used to fit the EIS data of cells with nonblocking electrodes, where Q is the constant phase element (CPE). Typical dimensions of the pellets were ~1.0 mm thick and 7.8 mm in diameter, with the heterostructured LLZO slightly thicker at ~2 mm. Cells with nonblocking electrodes were cycled at ambient temperature inside an Ar-filled glovebox at a constant current density of 46 $\mu A/cm^2$ for 20 cycles (2 h per cycle) or varying current densities for 4 cycles (1 h per cycle). The current density started at 46 $\mu A/cm^2$ and was stepped in increments of 22 $\mu A/cm^2$ until cell shorting occurred. A rest period of ~30 min was used between each current step.

The Laue X-ray microdiffraction experiments were conducted at Beamline 12.3.2 of the Advanced Light Source (ALS) at Lawrence Berkeley National Laboratory. A polychromatic X-ray beam (5−22 keV) was focused to ~1 × 1 μm^2 by a pair of Kirkpatrick−Baez mirrors. The sample was mounted on a high resolution $x−y$ scan stage and tilted 45° relative to the incident X-ray beam. Laue diffraction images were recorded in reflection mode with a two-dimensional Pilatus-1 M detector mounted at 90° to the incoming X-ray, approximately 140 mm from the probe spot. Exposure time at each position was 1 s. The sharp reflections indicate a relatively low dislocation density within the probed diffraction volume (~1 × 1 × 40 μm^3). The detector has a pixel size of 0.17 mm. Peak positions were determined by fitting of a 2d Gaussian function with a precision of about 0.1 pixels, providing an angular resolution of ~0.01°. Calibrations for distance, center channel position, and tilt of detector were performed on the basis of a Laue pattern from a strain-free synthetic quartz crystal exhibiting similar penetration characteristics as LLZO. This takes into account absorption and extinction effects. For the LLZO_LG pellet, a 2-D scan of 67 × 67 points was performed with a step size of 15 μm, and for the LLZO_SG pellet, a scan of 167 × 167 points was performed with a step size of 6 μm. Thus, similar amounts of data points per grain were collected for both the small- and large-grained samples. The X-ray scan diffraction data was then processed by XMAS software.[34]

RESULTS AND DISCUSSION

Figure 1 shows a schematic of the processing routes we developed to fabricate densified LLZO pellets with a variety of complex microstructures. To achieve densification of LLZO pellets with different microstructures under the same thermal conditions, the key is to control the particle size distribution in the packed green body by using a bimodal distribution, i.e., mixing large particles with smaller ones. As reported in our previous work, densification of the pellet green body made entirely of smaller particles of 1−2 μm is associated with tremendous grain growth.[17] Sintered pellets typically exhibited grain sizes of 100−200 μm (~100 times growth) and 92% theoretical density, suggesting that a liquid sintering process might be actively involved.[25] Figure 2a,b shows SEM images of the surface morphologies and fractured cross sections of sintered pellets made from different weight ratios of small and large particles. Introducing a small amount of larger particles with an average diameter of 10 μm into the small particles (~1 μm diameter) in the green body effectively suppressed the grain growth, resulting in dense pellets with a much decreased grain
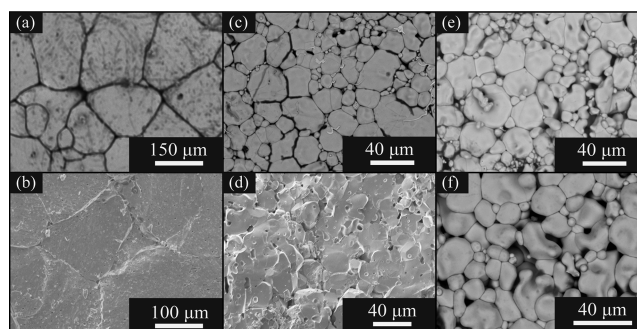

Figure 2. SEM images of (a) surface morphology of a sintered pellet made from 1 μm LLZO particles, (b) cross-section of a sintered pellet made from 1 μm LLZO particles, (c) surface morphology of a sintered pellet made from a mixture of 1 and 10 μm LLZO particles in a 90:10 weight ratio, (d) cross-section of a sintered pellet made from 90 wt % 1 μm particles and 10 wt % 10 μm particles, (e) surface morphology of a sintered pellet made from a mixture of 1 and 10 μm LLZO particles in a 70:30 weight ratio, and (f) surface morphology of a sintered pellet made from a mixture of 1 and 10 μm LLZO particles in a 50:50 weight ratio.

size of about 20−40 μm across. A systematic study of the densification of the packed green bodies consisting of bimodal distributions of particles with different ratios of 10 μm-sized particles (10, 30, and 50 wt %) was carried out. In all cases, the large grain growth seen when only fine powders were used was suppressed. When the 10 μm size particle content was 10 wt %, the green body was reasonably well-sintered (Figure 2c) with a relative density of 90%, close to the 92% found for pellets made exclusively from fine particles. The pellet exhibited a distribution of grain sizes, with large ones about 20−40 μm across surrounded by pockets of smaller ones less than 10 μm in size. Fractured cross-section images of the pellets made from 10 wt % 10 μm particles are provided in Figure 2d. In comparison, densification was inhibited when larger amounts of the 10 μm particles were used in the bimodal mixture. Specifically, the surface of the pellet made with 30 wt % large particles in the mixture exhibited a distribution of small grains 4−5 μm across along with larger grains about 30 μm in size (Figure 2b). The pellet had an estimated relative density of 80%. Increasing the content of the 10 μm particles in the green body resulted in poorer densification (Table S1 in Supporting Information) of the sintered pellets. For the 50 wt % mixture, the pellet was not fully sintered; the open porosity is clearly visible in Figure 2f, and the grain size is between 10 and 20 μm. Because of their high relative densities, only pellets made from 90 wt % fine powder (90% density) with grain sizes averaging 20−40 μm across (designated as LLZO_SG) and pellets made from 100% fine powder (92% density) with grain sizes about 100−200 μm across (designated as LLZO_LG) were subjected to further study. In both cases, only closed and isolated pores were observed within the pellets. Inductively coupled plasma optical emission spectroscopy (ICP-OES) indicated that the overall chemical compositions of the two samples were similar: the chemical compositions are $Li_{5.98}Al_{0.33}La_3Zr_{1.95}O_{11.89}$ and $Li_{5.92}Al_{0.36}La_3Zr_{1.96}O_{11.92}$ for LLZO_SG and LLZO_LG, respectively. (Oxygen content was estimated from charge neutrality considerations.) This is not surprising since LLZO_SG and LLZO_LG pellets were both subjected to the same thermal treatment of sintering at 1100 °C for 12 h. The lattice parameters derived from the XRD patterns were also similar at 12.964(6) Å for LLZO_SG and 12.963(7) Å for

LLZO_LG, further confirming comparable overall chemical compositions. Chemical compositions by ICP-OES and lattice parameters are provided in Tables S2 and S3, Supporting Information.[17,35]

By exploiting the uniquely different densified microstructures of LLZO_LG and LLZO_SG samples, it was possible to fabricate LLZO solid electrolytes with complex heterostructures. This was carried out by pressing and cosintering three alternating layers of green bodies composed of either the 90/10 bimodal distribution of 1 and 10 μm particles, or entirely consisting of 1 μm particles. Figure 3 shows cross-section SEM
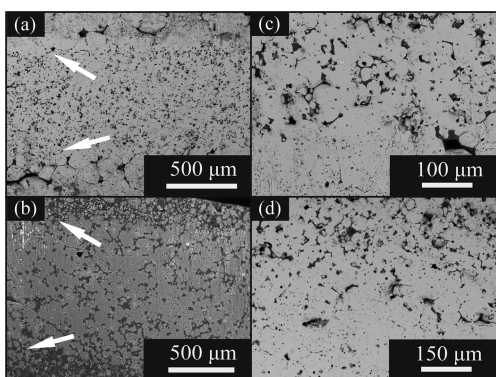
Figure 3. SEM cross-section images of (a) LLZO_LG/SG/LG heterostructure, (b) LLZO_SG/LG/SG heterostructure, (c) magnified junction region of LG/SG/LG heterostructure, and (d) magnified junction region of SG/LG/SG heterostructure. (Arrows indicate positions of junction regions.)

images of the pellets with an approximately 1 mm thick inner layer of small grains sandwiched between 300 μm thick surface layers of larger grains (designated LLZO_LG/SG/LG, Figure 3a) and an approximately 1 mm thick inner layer with large grains sandwiched between 200 and 300 μm thick surface layers with small grains (designated LLZO_SG/LG/SG, Figure 3b). SEM images of polished cross sections at the layer junctions of LLZO_LG/SG/LG and LLZO_SG/LG/SG are shown in Figure 3c,d, respectively. In the LLZO_LG/SG/LG pellet, large grains of about 200 μm are visible on the bottom and smaller grains of 20−40 μm on top. Larger grains of ~400 μm were also observed on the surface layer of the LLZO_LG/SG/LG sample. The enhanced grain growth might be associated with the induced stress/strain of mismatched sintering of the alternating layers. In the LLZO_SG/LG/SG sample, large grains of 100 μm can be easily observed, tightly bonded with

the layer composed of 20−40-μm-sized grains. The densities of the LLZO_LG/SG/LG and SG/LG/SG heterostructures were 89% and 90%, respectively.

Total ionic conductivities of both LLZO_LG and LLZO_SG pellets are plotted versus temperature in Figure 4a. The total ionic conductivity at room temperature and activation energy of LLZO_SG were measured to be 2.5×10^{-4} S/cm and 0.34 eV, slightly higher than the 2.0×10^{-4} S/cm and 0.32 eV found for LLZO_LG (summarized in Table 1). This observation agrees

Table 1. Total Ionic Conductivity at 25 °C, Activation Energy, and Interfacial Area Specific Resistances (ASRs) of LLZO Pellets as a Function of Microstructure

| pellet	total conductivity (S/cm)	activation energy (eV)	ASR (Ω cm^2)
LLZO_SG	2.5×10^{-4}	0.34	37
LLZO_LG	2.0×10^{-4}	0.32	130
SG/LG/SG	n/a	n/a	51
LG/SG/LG	n/a	n/a	227

well with the fact that higher activation energies have been measured for grain boundaries than in the bulk for several lithium ion conductors, and that LLZO_SG has a higher concentration of grain boundaries than LLZO_LG.[15,17,36] Indeed, Tenhaeff et al.[37] have resolved the different contributions of ionic conduction in bulk and grain boundaries in a hot pressed LLZO solid electrolyte. They reported that bulk resistance dominates at temperatures higher than −10 °C, suggesting that the grain boundary network conducts better than grains at temperatures above this point. It has also been observed that the ionic conductivity of nanocrystalline LLZO is enhanced, due to the very small grain sizes and larger concentration of grain boundaries.[24]

In the case of the LLZO_SG samples, the ionic conductivity at room temperature was only moderately improved compared to LLZO_LG. However, the LLZO/Li interfacial transport was much better. For the measurement of the interfacial resistances, LLZO_SG and LLZO_LG pellets were polished in the same way to minimize the difference of surface roughness and sandwiched between lithium electrodes. Figure S2, Supporting Information, shows SEM images of the surface morphologies of LLZO_LG and LLZO_SG pellets after polishing. Both of the cells containing LLZO_LG and LLZO_SG showed one partial semicircle in the high frequency range and a complete semicircle at lower frequencies in the Nyquist plots (Figure 4b). The semicircles at high frequencies can be assigned to the
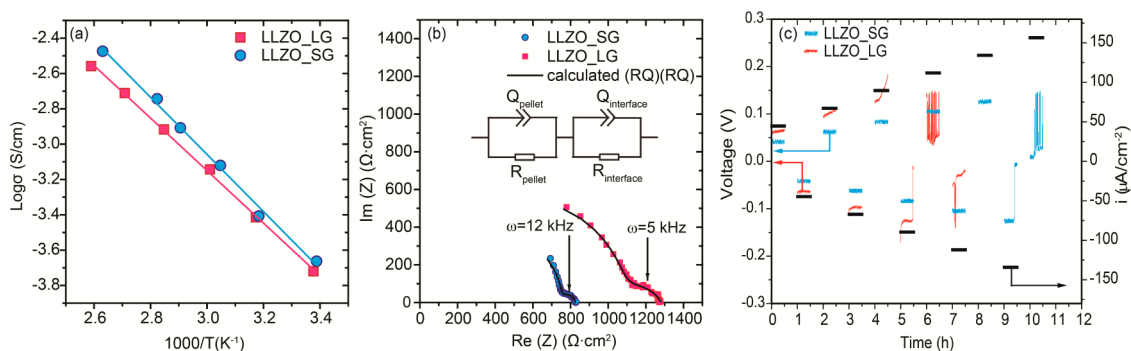
Figure 4. (a) Arrhenius plot of total ionic conductivity; (b) Nyquist plot of Li/LLZO/Li symmetrical cells; (c) galvanostatic cycling of Li/LLZO/Li symmetrical cells, stepping the current density from 46 to 156 μA cm^{-2}, with a step size of 22 μA cm^{-2}.
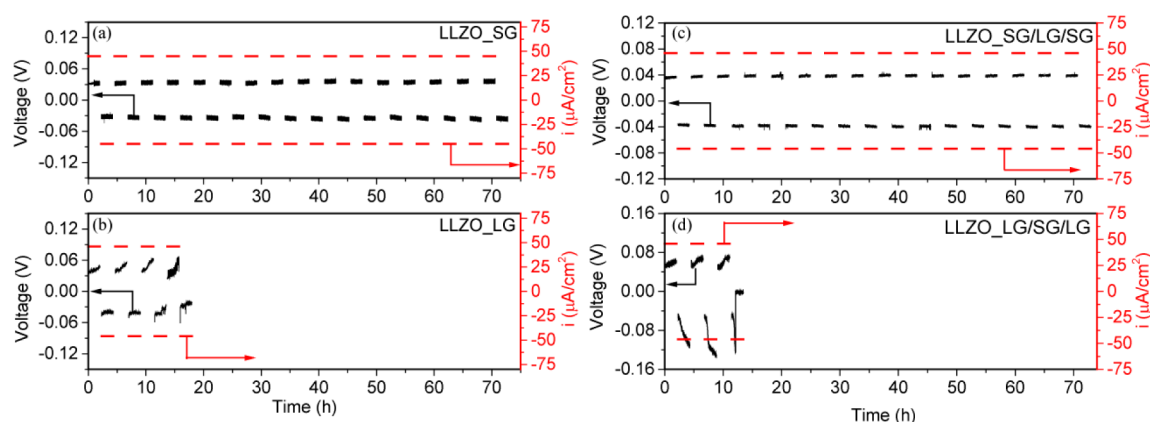
Figure 5. Galvanostatic cycling of symmetrical cells at constant current densities of ± 46 μA cm^{-2} of (a) Li/LLZO_SG/Li, (b) Li/LLZO_LG/Li, (c) Li/LLZO_SG_LG_SG/Li, and (d) Li/LLZO_LG_SG_LG/Li.

total resistance of the LLZO pellets on the basis of comparison to the data obtained on cells with blocking electrodes, and the low frequency semicircles are attributable to the resistances of the Li/LLZO interfaces.[15,38] The interface area specific resistance (ASR) for Li/LLZO_SG was only 37 Ω cm^2, one-third the value of LLZO_LG (130 Ω cm^2).[13,14,19−21,39] Nyquist fitting results are provided in Table S4, Supporting Information. Furthermore, this indicates that high interfacial resistances are not intrinsic to Li/LLZO cells but are strongly correlated with the grain size and can be reduced by engineering of the microstructure and grain boundaries.

In addition to decreasing the interfacial resistance, the proper microstructure also positively impacts the cycling behavior. A comparison of cycling performances using dc stepped current cycling of symmetrical lithium cells containing LLZO_SG and LLZO_LG pellets is shown in Figure 4c. The cell containing LLZO_SG performed much better in all aspects: critical current density, overpotential, and cycling lifetime. The potential of the Li/LLZO_SG/Li symmetrical cell remains constant at |∼0.04 V| at current densities of ± 46 μA cm^{-2} and increased linearly at higher current densities. The potential agrees with the value predicted by ac impedance experiments, indicating that the primary charge carriers are lithium ions. The voltage profile during each step is flat for all current densities up to 134 μA cm^{-2}, typical of the behavior of single ion conductors. Above this value, the cell exhibited voltage instability and short circuited, consistent with the formation of Li dendrites.[19] Thus, the critical current density for the cell containing the LLZO_SG pellet was 134 μA cm^{-2}. In comparison, the cell containing the LLZO_LG pellet showed an unstable potential even at the lowest current density tested (46 μA cm^{-2}). This is probably a consequence of an overpotential increase due to significantly slower interfacial ionic transport in LLZO_LG than LLZO_SG. The phenomenon is more severe at higher current densities. An overpotential as high as ∼0.08 V rapidly accumulated for this cell when the current density was raised to 90 μA cm^{-2} and the cell shorted during the 2 h period at this current density. Thus, the critical current density was only 90 μA cm^{-2} compared to 134 μA cm^{-2} for the cell containing LLZO_SG.

We speculated that the lower resistance at the interface between Li and LLZO associated with the surface microstructure of LLZO_SG accounted for the improved electrochemical properties. However, solely on the basis of the experiments presented in Figure 4, we could not rule out bulk effects. For this reason, we prepared the two different types of heterostructures described earlier, which had thin surface regions with different microstructures from those in the thicker interior (Figure 3). The role of the surface microstructure could then be compared by measuring symmetrical cells containing the two different heterostructures: the one with the large grains on the outside (LG/SG/LG) and the one with small grains outside (SG/LG/SG). The interfacial ASRs of the symmetrical cells containing the heterostructured pellets are given in Table 1. While the ASR for the cell containing LLZO_SG/LG/SG is 51 Ω cm^2, slightly higher than the 37 Ω cm^2 measured for LLZO_SG, the value increased to 227 Ω cm^2 for LLZO_LG/SG/LG, which is higher than that found in the LLZO_LG. This higher value may be related to the presence of the very large grains 400 μm across at the surfaces of the LLZO_LG/SG/LG pellet. The study confirms that the interfacial resistance between Li and LLZO is lower when the surface of the LLZO has a finer microstructure and more grain boundaries. The cycling performances of cells containing LLZO_SG, LLZO_LG, LLZO_LG/SG/LG, and LLZO_SG/LG/SG solid electrolytes at a constant current density of 46 μA cm^{-2} are shown in Figure 5. The cells containing LLZO_SG and LLZO_SG/LG/SG behaved similarly: at ± 46 μA cm^{-2}, both cycled stably with potentials of |0.03 V| and |0.04 V|, respectively, for more than 72 h with no signs of voltage instability or short-circuiting. Cells with LLZO_LG and LLZO_LG/SG/LG exhibited poor performance at the same current density: the cells exhibited voltage instability, fast overpotential build-up, and short-circuited within 20 and 15 h, respectively. The data for the cells containing LLZO_LG and LLZO_LG/SG/LG suggest that the severe buildup of overpotential during dc cycling is related to slow ionic transport in the interface regions at the surface layers, which are composed of large grains.[21] The short cycle lives of the cells containing LLZO with large grains at the surfaces may be explained by detrimental current focusing due to inhomogeneous current distributions, which causes rapid initiation of lithium dendrites at interfaces, a phenomenon extensively studied in sodium beta alumina in the 1970−1980s.[40−44]

At LLZO/Li interfaces, the dc ionic current flow is inhomogeneous because of differences between the resistivities of the surface grains and grain boundaries. The lithium ion current redistributes in such a way that low resistivity paths are favored and can lead to dendrite formation. Lithium transport is known for its dependence on crystal facet orientation, which

may further impact current distribution in polycrystalline electrolytes. For example, Kim et al. observed that the ionic conductivity varied with crystal orientation in epitaxial garnet type electrolyte films.[45] A wide distribution of intergranular/ grain-boundary resistivities could also play an active role, as highly conductive boundaries are favored for lithium ion transport over more resistive boundaries and bulk grains. Thus, information pertaining to grain orientations and grain boundary misorientations is critical in determining their contribution to the observed electrochemical behavior. To this end, X-ray Laue microdiffraction was used to probe the grain orientation and grain boundary misorientation distribution in the top layer of surface grains in the LLZO_SG and LLZO_LG solid electrolyte samples over a relatively large area (1 mm²).[46] The technique uses white beam energy between 6 and 22 keV with a maximum X-ray penetration depth of 15 μm. The surface grain sensitivity is assured by the indexing algorithm which ranks the measured reflections according to their intensities, thus preferring surface grains over subsurface grains whose reflection intensities are reduced by absorption of the surface grains. A representative Laue diffraction pattern for LLZO is shown in Supporting Information Figure S3. Histograms of the grain orientations of the LLZO_LG and LLZO_SG samples are presented in Figure 6a, and grain
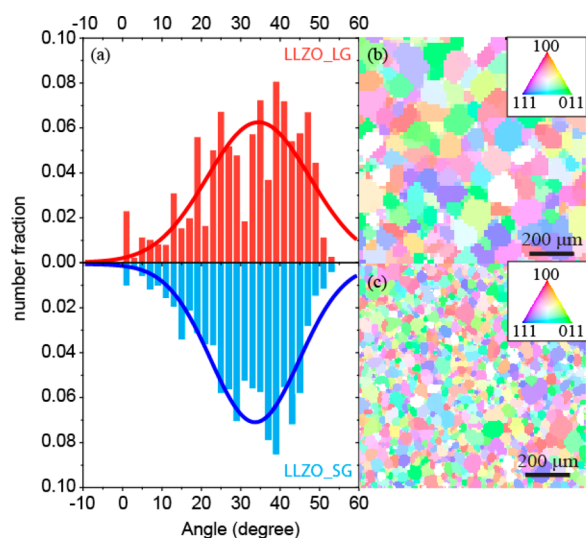

Figure 6. (a) Histograms of angles between grain orientation (100) direction and sample plane normal for LLZO_LG (top) and LLZO_SG (bottom). (b) Grain orientation mapping of LLZO_LG. (c) Grain orientation mapping of LLZO_SG.

orientation maps (1 mm × 1 mm area) are displayed in Figure 6b,c for LLZO_LG and LLZO_SG, respectively. Neither the histogram nor the grain orientation map reveals notable differences in LLZO_LG and LLZO_SG. For both samples, the grain orientation is largely random. The mean grain orientation angle between the (100) direction and sample normal is 31.90° with a standard deviation of 12.19° for LLZO_LG and 31.48° with a standard deviation of 11.09° for LLZO_SG. The similar grain orientation distributions in the two cases, therefore, do not contribute to the observed differences in the electrochemical performance.

It has been reported that low angle grain boundaries are preferred ion transport pathways over high angle ones since the latter are energetically unstable, leading to radical local

structure and composition deviations as observed in lithium lanthanum titanate (LLTO) and LATP.[47,48] The distribution of grain boundaries was analyzed by determining misorientation angles between neighboring grains. The mean misorientation angle of LLZO_SG is 37.83° with a standard deviation of 14.70° while it is 39.40° with a standard deviation of 13.60° for LLZO_LG (Figure 7). The similar values suggest that the
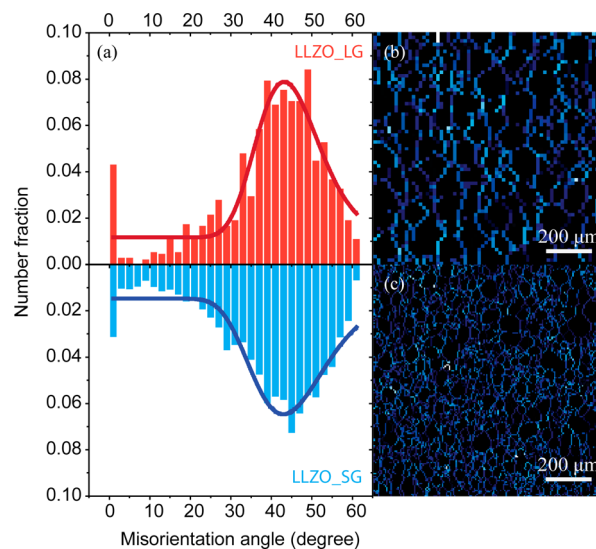
Figure 7. (a) Histograms of misorientation angles for LLZO_LG (top) and LLZO_SG (bottom); (b, c) misorientation angle mapping of LLZO_LG and LLZO_SG.

improved electrochemical properties in LLZO_SG compared to LLZO_LG are not attributable to differences in grain boundaries distributions. It should, however, be noted that glassy or crystalline secondary phases can form in energetically unfavorable boundaries with typical thicknesses in the range 2– 100 nm,[31,49] beyond the resolution of the 1 μm X-ray beam of the μXRD experiment. In Al-substituted LLZO, these phases are generally Al rich segregates that are less conductive than the main phase.[17,31,50,51] Upon sintering LLZO_SG and LG, the formation and distribution of these Al containing segregates may vary, adding extra complexity in determining the current distribution. One possibility is that the blocking segregates may be more uniformly distributed inside LLZO_SG compared to the LLZO_LG sample, accounting for its better electrochemical cycling behavior. High resolution transmission electron microscopy is required for detailed observation of the local structure and chemistry of grain boundary impurities, which needs special precautions, such as fast scan rates and diffused irradiation area, to avoid electron beam damage in materials with highly mobile lithium ions.[47,52]

Because both the grain orientation and grain boundary misorientation do not show notable differences in our study, the improved interfacial resistance and cycling performance observed in cells containing LLZO_SG can be attributed to a larger area fraction of low resistivity grain boundaries at the LLZO surfaces compared to LLZO_LG. The total surface grain boundary area fraction is 32.2% for LLZO_SG and 16.5% for LLZO_LG, as estimated from SEM images (Figure S4, Supporting Information). The larger area of grain boundaries with low resistivity in LLZO_SG effectively dissipates the ionic current densities and improves the ion transport when interfaced with lithium metal electrodes. Further evidence for

the greater conductivity of the grain boundaries was observed in optical microscopy images of an LLZO_LG sample taken from a shorted cell (Figure S5, Supporting Information). For this experiment, two lithium electrodes were placed on ends of a bar-shaped sample of LLZO. Before cycling, the bar was uniformly ivory colored in appearance. After short-circuiting, black features developed from one side of the bar to the other. Upon magnification, it can be clearly seen that the blackening occurred along the grain boundaries. Similar results have been observed in previous experiments, and have been attributed to dendrite formation.[19] Dendrites form due to current focusing at the more highly conductive grain boundaries.

CONCLUSIONS

We directly correlated the microstructures of solid ceramic electrolytes with interfacial resistances and cycling performance in symmetrical cells containing them, using Al substituted LLZO as a model system. We demonstrated a simple processing route for fabrication of complex LLZO hetero-structures with controlled compositions and microstructures. A very low interfacial resistance of 37 Ω cm^2 and greatly improved cycling performances were achieved for cells containing samples with grain sizes about 20−40 μm across compared to those with larger grains. Our electrochemical results suggested that the type of microstructure at the solid electrolyte surface, which interfaces with the lithium metal electrodes, is crucial to the transport properties and the cycling life of the solid electrolyte. This was confirmed by using complex hetero-structures, in which the surfaces of the dense samples had differing microstructures than the bulk. High-resolution synchrotron X-ray Laue microdiffraction was also used to probe and map the distributions of grain orientation and misorientations of neighboring grains. No significant differences were observed between samples with small grains and those with large grains. Thus, we conclude that the better performance observed for small-grained samples can be attributed to the larger relative amount of surface layer grain boundaries, rather than grain orientation and grain boundary misorientation effects. The electrochemical properties, especially interfacial resistances and electrical cycling performance of dense LLZO solid electrolytes in lithium cells, are strongly influenced by the microstructures and grain boundaries at the interfaces. These insights indicate that LLZO solid electrolytes should have small grains and multiple grain boundaries to ensure the successful development of durable high-energy lithium metal batteries containing them. Further work will be directed toward understanding the enhanced ionic transport at the grain boundaries, particularly their chemical and structural natures.

ASSOCIATED CONTENT

Ⓢ Supporting Information

Additional details including densities of sintered heterostructures, ICP element analysis, lattice parameter, XRD patterns, EIS fitting results, and SEM images of polished pellet surface. This material is available free of charge via the Internet at http://pubs.acs.org.

AUTHOR INFORMATION

Corresponding Authors

*E-mail: leicheng@lbl.gov.
*E-mail: mmdoeff@lbl.gov.

Notes

ACKNOWLEDGMENTS

REFERENCES

(1) Girishkumar, G.; McCloskey, B.; Luntz, A. C.; Swanson, S.; Wilcke, W. Lithium−Air Battery: Promise and Challenges. *J. Phys. Chem. Lett.* **2010**, *1*, 2193−2203.

(2) Ji, X.; Lee, K. T.; Nazar, L. F. A Highly Ordered Nanostructured Carbon-Sulphur Cathode for Lithium-Sulphur Batteries. *Nat. Mater.* **2009**, *8*, 500−506.

(3) Gallagher, K. G.; Goebel, S.; Greszler, T.; Mathias, M.; Oelerich, W.; Eroglu, D.; Srinivasan, V. Quantifying the Promise of Lithium−Air Batteries for Electric Vehicles. *Energy Environ. Sci.* **2014**, *7*, 1555.

(4) Xu, W.; Wang, J.; Ding, F.; Chen, X.; Nasybulin, E.; Zhang, Y.; Zhang, J.-G. Lithium Metal Anodes for Rechargeable Batteries. *Energy Environ. Sci.* **2014**, *7*, 513.

(5) Takada, K. Progress and Prospective of Solid-State Lithium Batteries. *Acta Mater.* **2013**, *61*, 759−770.

(6) Aono, H. Ionic Conductivity of Solid Electrolytes Based on Lithium Titanium Phosphate. *J. Electrochem. Soc.* **1990**, *137*, 1023.

(7) Knauth, P. Inorganic Solid Li Ion Conductors: An Overview. *Solid State Ionics* **2009**, *180*, 911−916.

(8) Kamaya, N.; Homma, K.; Yamakawa, Y.; Hirayama, M.; Kanno, R.; Yonemura, M.; Kamiyama, T.; Kato, Y.; Hama, S.; Kawamoto, K.; Mitsui, A. A Lithium Superionic Conductor. *Nat. Mater.* **2011**, *10*, 682−686.

(9) Hartmann, P.; Leichtweiss, T.; Busche, M. R.; Schneider, M.; Reich, M.; Sann, J.; Adelhelm, P.; Janek, J. Degradation of NASICON-Type Materials in Contact with Lithium Metal: Formation of Mixed

Conducting Interphases (MCI) on Solid Electrolytes. *J. Phys. Chem. C* **2013**, *117*, 21064−21074.

(10) Ong, S. P.; Mo, Y.; Richards, W. D.; Miara, L.; Lee, H. S.; Ceder, G. Phase Stability, Electrochemical Stability and Ionic Conductivity of the $Li_{10\pm1}MP_2X_{12}$ (M = Ge, Si, Sn, Al or P, and X = O, S or Se) Family of Superionic Conductors. *Energy Environ. Sci.* **2013**, *6*, 148.

(11) Murugan, R.; Thangadurai, V.; Weppner, W. Fast Lithium Ion Conduction in Garnet-Type $Li_7La_3Zr_2O_{12}$. *Angew. Chem., Int. Ed.* **2007**, *46*, 7778−7781.

(12) Thangadurai, V.; Narayanan, S.; Pinzaru, D. Garnet-Type Solid-State Fast Li Ion Conductors for Li Batteries: Critical Review. *Chem. Soc. Rev.* **2014**, *43*, 4714−4727.

(13) Rangasamy, E.; Sahu, G.; Keum, J.; Rondinone, A.; Dudney, N.; Liang, C. A High Conducting Oxide-Sulfide Composite Lithium Superionic Conductor. *J. Mater. Chem. A* **2014**, *2*, 4111−4116.

(14) Liu, Z.; Fu, W.; Payzant, E. A.; Yu, X.; Wu, Z.; Dudney, N. J.; Kiggans, J.; Hong, K.; Rondinone, A. J.; Liang, C. Anomalous High Ionic Conductivity of Nanoporous β-Li_3PS_4. *J. Am. Chem. Soc.* **2013**, *135*, 975−978.

(15) Buschmann, H.; Dölle, J.; Berendts, S.; Kuhn, A.; Bottke, P.; Wilkening, M.; Heitjans, P.; Senyshyn, A.; Ehrenberg, H.; Lotnyk, A.; et al. Structure and Dynamics of the Fast Lithium Ion Conductor "$Li_7La_3Zr_2O_{12}$". *Phys. Chem. Chem. Phys.* **2011**, *13*, 19378−19392.

(16) Ohta, S.; Komagata, S.; Seki, J.; Saeki, T.; Morishita, S.; Asaoka, T. All-Solid-State Lithium Ion Battery Using Garnet-Type Oxide and Li_3BO_3 Solid Electrolytes Fabricated by Screen-Printing. *J. Power Sources* **2013**, *238*, 53−56.

(17) Cheng, L.; Park, J. S.; Hou, H.; Zorba, V.; Chen, G.; Richardson, T.; Cabana, J.; Russo, R.; Doeff, M. Effect of Microstructure and Surface Impurity Segregation on the Electrical and Electrochemical Properties of Dense Al-Substituted $Li_7La_3Zr_2O_{12}$. *J. Mater. Chem. A* **2014**, *2*, 172.

(18) Kotobuki, M.; Munakata, H.; Kanamura, K.; Sato, Y.; Yoshida, T. Compatibility of $Li_7La_3Zr_2O_{12}$ Solid Electrolyte to All-Solid-State Battery Using Li Metal Anode. *J. Electrochem. Soc.* **2010**, *157*, A1076.

(19) Sudo, R.; Nakata, Y.; Ishiguro, K.; Matsui, M.; Hirano, A.; Takeda, Y.; Yamamoto, O.; Imanishi, N. Interface Behavior between Garnet-Type Lithium-Conducting Solid Electrolyte and Lithium Metal. *Solid State Ionics* **2014**, *262*, 151−154.

(20) Ishiguro, K.; Nakata, Y.; Matsui, M.; Uechi, I.; Takeda, Y.; Yamamoto, O.; Imanishi, N. Stability of Nb-Doped Cubic $Li_7La_3Zr_2O_{12}$ with Lithium Metal. *J. Electrochem. Soc.* **2013**, *160*, A1690−A1693.

(21) Cheng, L.; Crumlin, E. J.; Chen, W.; Qiao, R.; Hou, H.; Franz Lux, S.; Zorba, V.; Russo, R.; Kostecki, R.; Liu, Z.; Persson, K.; Yang, W.; Cabana, J.; Richardson, T. J.; Chen, G.; Doeff, M. M. The Origin of High Electrolyte-Electrode Interfacial Resistances in Lithium Cells Containing Garnet Type Solid Electrolytes. *Phys. Chem. Chem. Phys.* **2014**, *16*, 18294−18300.

(22) Harris, S. J.; Lu, P. Effects of Inhomogeneities—Nanoscale to Mesoscale—on the Durability of Li-Ion Batteries. *J. Phys. Chem. C* **2013**, *117*, 6481−6492.

(23) Barsoum, M. *Science and Technology of Fast Ion Conductors*; Tuller, H. L., Balkanski, M., Eds.; NATO ASI Series; Springer: Boston, MA, 1990; Chapter 9, pp 241−270.

(24) Sakamoto, J.; Rangasamy, E.; Kim, H.; Kim, Y.; Wolfenstine, J. Synthesis of Nano-Scale Fast Ion Conducting Cubic $Li_7La_3Zr_2O_{12}$. *Nanotechnology* **2013**, *24*, 424005.

(25) Jin, Y.; McGinn, P. J. $Li_7La_3Zr_2O_{12}$ Electrolyte Stability in Air and Fabrication of a Li/$Li_7La_3Zr_2O_{12}$/$Cu_{0.1}V_2O_5$ Solid-State Battery. *J. Power Sources* **2013**, *239*, 326−331.

(26) Buschmann, H.; Berendts, S.; Mogwitz, B.; Janek, J. Lithium Metal Electrode Kinetics and Ionic Conductivity of the Solid Lithium Ion Conductors "$Li_7La_3Zr_2O_{12}$" and $Li_{7-x}La_3Zr_{2-x}Ta_xO_{12}$ with Garnet-Type Structure. *J. Power Sources* **2012**, *206*, 236−244.

(27) Huang, M.; Liu, T.; Deng, Y.; Geng, H.; Shen, Y.; Lin, Y.; Nan, C.-W. Effect of Sintering Temperature on Structure and Ionic Conductivity of $Li_{7-x}La_3Zr_2O_{12-0.5x}$ (x=0.5∼0.7) Ceramics. *Solid State Ionics* **2011**, *204−205*, 41−45.

(28) Rettenwander, D.; Geiger, C. A.; Tribus, M.; Tropper, P.; Amthauer, G. A Synthesis and Crystal Chemical Study of the Fast Ion Conductor $Li_{7-3x}Ga_xLa_3$ Zr_2O_{12} with X = 0.08 to 0.84. *Inorg. Chem.* **2014**, *53*, 6264−6269.

(29) Rangasamy, E.; Wolfenstine, J.; Sakamoto, J. The Role of Al and Li Concentration on the Formation of Cubic Garnet Solid Electrolyte of Nominal Composition $Li_7La_3Zr_2O_{12}$. *Solid State Ionics* **2012**, *206*, 28−32.

(30) Murugan, R.; Thangadurai, V.; Weppner, W. Effect of Lithium Ion Content on the Lithium Ion Conductivity of the Garnet-like Structure $Li_{5+x}BaLa_2Ta_2O_{11.5+0.5x}$ (x = 0−2). *Appl. Phys. A: Mater. Sci. Process.* **2008**, *91*, 615−620.

(31) Li, Y.; Wang, Z.; Li, C.; Cao, Y.; Guo, X. Densification and Ionic-Conduction Improvement of Lithium Garnet Solid Electrolytes by Flowing Oxygen Sintering. *J. Power Sources* **2014**, *248*, 642−646.

(32) Rettenwander, D.; Blaha, P.; Laskowski, R.; Schwarz, K.; Bottke, P.; Wilkening, M.; Geiger, C. A.; Amthauer, G. DFT Study of the Role of Al^{3+} in the Fast Ion-Conductor $Li_{7-3X}Al_{3+X}La_3Zr_2O_{12}$ Garnet. *Chem. Mater.* **2014**, *26*, 2617−2623.

(33) Geiger, C. A.; Alekseev, E.; Lazic, B.; Fisch, M.; Armbruster, T.; Langner, R.; Fechtelkord, M.; Kim, N.; Pettke, T.; Weppner, W. Crystal Chemistry and Stability of "$Li_7La_3Zr_2O_{12}$" Garnet: A Fast Lithium-Ion Conductor. *Inorg. Chem.* **2011**, *50*, 1089−1097.

(34) Tamura, N. XMAS: A Versatile Tool for Analyzing Synchrotron X-Ray Microdiffraction Data (World Scientific). In *Strain and Dislocation Gradients from Diffraction*; Barabash, R., Ice, G., Eds.; Imperial College Press: London,2014; Chapter 4, pp 125−155.

(35) Djenadic, R.; Botros, M.; Benel, C.; Clemens, O.; Indris, S.; Choudhary, A.; Bergfeldt, T.; Hahn, H. Nebulized Spray Pyrolysis of Al-Doped $Li_7La_3Zr_2O_{12}$ Solid Electrolyte for Battery Applications. *Solid State Ionics* **2014**, *263*, 49−56.

(36) Mariappan, C. R.; Gellert, M.; Yada, C.; Rosciano, F.; Roling, B. Grain Boundary Resistance of Fast Lithium Ion Conductors: Comparison between a Lithium-Ion Conductive Li−Al−Ti−P−O-Type Glass Ceramic and a $Li_{1.5}Al_{0.5}Ge_{1.5}P_3O_{12}$ Ceramic. *Electrochem. Commun.* **2012**, *14*, 25−28.

(37) Tenhaeff, W. E.; Rangasamy, E.; Wang, Y.; Sokolov, A. P.; Wolfenstine, J.; Sakamoto, J.; Dudney, N. J. Resolving the Grain Boundary and Lattice Impedance of Hot-Pressed $Li_7La_3Zr_2O_{12}$ Garnet Electrolytes. *ChemElectroChem* **2013**, *1*, 375−378.

(38) Zhang, L.; Cheng, L.; Cabana, J.; Chen, G.; Doeff, M. M.; Richardson, T. J. Effect of Lithium Borate Addition on the Physical and Electrochemical Properties of the Lithium Ion Conductor $Li_{3.4}Si_{0.4}P_{0.6}O_4$. *Solid State Ionics* **2013**, *231*, 109−115.

(39) Buschmann, H.; Dolle, J.; Berendts, S.; Kuhn, A.; Bottke, P.; Wilkening, M.; Heitjans, P.; Senyshyn, A.; Ehrenberg, H.; Lotnyk, A.; Duppel, V.; Kienle, L.; Janek, J. Structure and Dynamics of the Fast Lithium Ion Conductor "$Li_7La_3Zr_2O_{12}$". *Phys. Chem. Chem. Phys.* **2011**, *13*, 19378−19392.

(40) Armstrong, R. D.; Dickinson, T.; Turner, J. The Breakdown of B-Alumina Ceramic Electrolyte. *Electrochim. Acta* **1974**, *19*, 187−192.

(41) De Jonghe, L. C. Grain Boundaries and Ionic Conduction in Sodium Beta Alumina. *J. Mater. Sci.* **1979**, *14*, 33−48.

(42) Ansell, R. The Chemical and Electrochemical Stability of Beta-Alumina. *J. Mater. Sci.* **1986**, *21*, 365−379.

(43) Buechele, A. C.; De Jonghe, L. C.; Hitchcock, D. Degradation of Sodium β''-Alumina: Effect of Microstructure. *J. Electrochem. Soc.* **1983**, *130*, 1042−1049.

(44) Feldman, L. A.; Jonghe, L. C. Initiation of Mode I Degradation in Sodium-Beta Alumina Electrolytes. *J. Mater. Sci.* **1982**, *17*, 517−524.

(45) Kim, S.; Hirayama, M.; Taminato, S.; Kanno, R. Epitaxial Growth and Lithium Ion Conductivity of Lithium-Oxide Garnet for an All Solid-State Battery Electrolyte. *Dalton Trans.* **2013**, *42*, 13112−13117.

(46) Kunz, M.; Tamura, N.; Chen, K.; MacDowell, A. A.; Celestre, R. S.; Church, M. M.; Fakra, S.; Domning, E. E.; Glossinger, J. M.; Kirschman, J. L.; Morrison, G. Y.; Plate, D. W.; Smith, B. V.; Warwick, T.; Yashchuk, V. V.; Padmore, H. A.; Ustundag, E. A Dedicated Superbend X-Ray Microdiffraction Beamline for Materials, Geo-, and

Environmental Sciences at the Advanced Light Source. *Rev. Sci. Instrum.* **2009**, *80*, 035108.

(47) Ma, C.; Chen, K.; Liang, C.; Nan, C.-W.; Ishikawa, R.; More, K.; Chi, M. Atomic-Scale Origin of the Large Grain-Boundary Resistance in Perovskite Li-Ion-Conducting Solid Electrolytes. *Energy Environ. Sci.* **2014**, *7*, 1638.

(48) Gellert, M.; Gries, K. I.; Yada, C.; Rosciano, F.; Volz, K.; Roling, B. Grain Boundaries in a Lithium Aluminum Titanium Phosphate-Type Fast Lithium Ion Conducting Glass Ceramic: Microstructure and Nonlinear Ion Transport Properties. *J. Phys. Chem. C* **2012**, *116*, 22675−22678.

(49) Aguesse, F.; López del Amo, J. M.; Roddatis, V.; Aguadero, A.; Kilner, J. A. Enhancement of the Grain Boundary Conductivity in Ceramic $Li_{0.34}La_{0.55}TiO_3$ Electrolytes in a Moisture-Free Processing Environment. *Adv. Mater. Interfaces* **2014**, *1*, 1300143.

(50) Ren, Y.; Deng, H.; Chen, R.; Shen, Y.; Lin, Y.; Nan, C.-W. Effects of Li Source on Microstructure and Ionic Conductivity of Al-Contained $Li_{6.75}La_3Zr_{1.75}Ta_{0.25}O_{12}$ Ceramics. *J. Eur. Ceram. Soc.* **2015**, *35*, 561−572.

(51) Park, J. S.; Cheng, L.; Zorba, V.; Mehta, A.; Cabana, J.; Chen, G.; Doeff, M. M.; Richardson, T. J.; Park, J. H.; Son, J.-W.; Hong, W.-S. Effects of Crystallinity and Impurities on the Electrical Conductivity of Li-La-Zr-O Thin Films. *Thin Solid Films* **2014**, DOI: 10.1016/j.tsf.2014.11.019.

(52) Lin, F.; Markus, I. M.; Doeff, M. M.; Xin, H. L. Chemical and Structural Stability of Lithium-Ion Battery Electrode Materials under Electron Beam. *Sci. Rep.* **2014**, *4*, 5694.